

# PCCP

Accepted Manuscript



This is an *Accepted Manuscript*, which has been through the Royal Society of Chemistry peer review process and has been accepted for publication.

*Accepted Manuscripts* are published online shortly after acceptance, before technical editing, formatting and proof reading. Using this free service, authors can make their results available to the community, in citable form, before we publish the edited article. We will replace this *Accepted Manuscript* with the edited and formatted *Advance Article* as soon as it is available.

You can find more information about *Accepted Manuscripts* in the [Information for Authors](#).

Please note that technical editing may introduce minor changes to the text and/or graphics, which may alter content. The journal's standard [Terms & Conditions](#) and the [Ethical guidelines](#) still apply. In no event shall the Royal Society of Chemistry be held responsible for any errors or omissions in this *Accepted Manuscript* or any consequences arising from the use of any information it contains.

## Thermostructural Behaviour of Ni-Cr Materials: Modelling Bulk and Nanoparticle Systems

Received 00th January 20xx,  
Accepted 00th January 20xx

DOI: 10.1039/x0xx00000x

www.rsc.org/

J. M. Ortiz-Roldan<sup>a</sup>, A. R. Ruiz-Salvador<sup>\*a</sup>, S. Calero<sup>a</sup>, F. Montero-Chacón<sup>b</sup>, E. García-Pérez<sup>b</sup>, J. Segurado<sup>c</sup>, I. Martín-Bragado<sup>c</sup>, and S. Hamad<sup>\*a</sup>

The thermostructural properties of Ni-Cr materials, as bulk and nanoparticle (NP) systems, have been predicted with a newly developed interatomic potential, for Ni/Cr ratios from 100/0 to 60/40. The potential, which has been fitted using experimental data and further validated using Density Functional Theory (DFT), describes correctly the variation with temperature of the lattice parameters and the coefficient of thermal expansion, from 100 K to 1000 K. Using this potential, we have performed Molecular Dynamics (MD) simulations on bulk Ni-Cr alloys of various compositions, for which no experimental data are available. Similarly, NPs with diameters of 3, 5, 7, 10 nm were studied. We found a very rapid convergence of NP properties with the size of the systems, showing already the 5 nm NPs a thermostructural behaviour similar to that the bulk. MD simulations of two 5 nm NPs show very little sintering and thermally-induced damage, for temperatures between 300 K and 1000 K, suggesting that materials formed by agglomeration of Ni-Cr NPs meet the thermostructural stability requirements for catalysis applications.

### 1 Introduction

Metal alloys have historically been used in structural applications, due to their exceptional mechanical properties. But the use of metals and metal alloys has been greatly extended during the last decades, in fields such as catalysis, medicine, engineering, electronics, etc.<sup>1</sup> This has been made possible thanks to the development of materials science, which has increased the range of properties of metallic systems. In many cases, there is an enhancement in specific properties upon alloying due to synergistic effects, and the rich diversity of compositions, structures, and properties of metal alloys and nanoalloys has led to widespread applications.<sup>2,3</sup>

Nickel-Chromium alloys are extensively used, mainly due to their excellent resistance to high temperature oxidation and corrosion.<sup>4</sup> There are six main nickel-based alloy groups, where chromium is the second main component in most of them. The role of chromium in corrosion-resistant nickel alloys is to enhance the formation of passive oxide films that impede the corrosion process.<sup>5</sup> This capability of nickel-chromium alloys is also largely exploited in energy related applications, where safety requirements demand high resistant for high temperature and/or pressure, as for example in nuclear power systems. In this sense, austenitic nickel-chromium-based alloys are also becoming widely extended within the aerospace industry (e.g. moving parts as rotors and blades, rocket nozzles and spacecraft shielding); chemical engineering (e.g. reactor shells, boilers or catalysts); or renewable energy (e.g. solar receivers, photovoltaic substrates) to cite a few. In fact, the development of this type of superalloys has become the core

business in some metallurgical companies. As a matter of fact, these superalloys are often referred to by their commercial names (e.g. Inconel<sup>®</sup>, Hastelloy<sup>®</sup>, Haynes<sup>®</sup>, or Chronin<sup>®</sup>).

Ni and Ni-Cr nanoparticles can be used for various applications, mainly in catalysis. For instance Ni nanoparticles catalyse the reactions to produce syngas by oxy-steam reforming of methane,<sup>6</sup> to produce hydrogen from bioethanol,<sup>7</sup> or to perform thermal decomposition of ammonia.<sup>8</sup> Ni nanoparticles can also be used in sensing applications,<sup>9,10</sup> and even in printed electronics.<sup>11</sup> There are still many hurdles for achieving more successful applications of Ni and Ni-Cr nanoparticles, such as the sintering of the nanoparticles, which decreases the surface to volume ratio of the system and modifies its morphology.<sup>12-14</sup> But for some applications, sintering can be a desirable effect, such as in the mentioned field of printed electronics.<sup>15</sup> It is then clear that a deep understanding of the dynamics of Ni and Ni-Cr nanoparticles is desirable.

But despite the relevance of Ni and Ni-Cr alloys, there are not available interatomic potentials appropriate for accurate modelling the thermo-structural properties of these materials at temperatures above room temperature. In this work we develop interatomic potentials with which to obtain an atomistic view of the behaviour of Ni and Ni-Cr bulk and nanoparticles. We have parametrized the potentials to obtain the best fit of a set of experimental observables, and we have subsequently carefully validated their performance. Using this potential, we are able to predict some properties of bulk Ni-Cr, for which there are no experimental data available. Finally, we used the potential to model Ni-Cr nanoparticles, of various sizes and Ni/Cr ratios, for a range of temperatures at which Ni-Cr alloys are commonly employed, namely between 300 K and 1000 K. MD simulations have become an invaluable source of information of the structural behaviour and deformation mechanisms of nanocrystalline metals.<sup>16</sup> The newly developed potential can be used in simulations of large systems, in order to get a better understanding of these materials, for instance by modelling whole nanoparticles, nanorods and nanotubes, among other nanostructures, as well as thin films and grain

<sup>a</sup> Department of Physical, Chemical, and Natural Systems, University Pablo de Olavide, Ctra. Utrera km. 1, 41013, Seville, Spain.

<sup>b</sup> Abengoa Research, Campus Palmas Altas, Calle Energía Solar 1, 41014, Seville, Spain.

<sup>c</sup> Instituto IMDEA Materiales, C/Eric Kandel 2, Tecnogatafe, 28906, Gatafe, Madrid, Spain.

† Footnotes relating to the title and/or authors should appear here. Electronic Supplementary Information (ESI) available: [details of any supplementary information available should be included here]. See DOI: 10.1039/x0xx00000x

boundary characterization or interface behaviour in polycrystals. Furthermore, this new potential can be the starting point for developing interatomic potentials with which to model inconels and other Ni-based alloys, by fitting the parameters for other metals, such as Fe, Co, or Mn.

## 2 Theoretical Methods

Embedded Atom Methods (EAM) provide a well-balanced description of metallic systems, due to their many-body nature capable of dealing reasonably well with metallic bonds.<sup>17, 18</sup> The energy of the system is described by:

$$E_{\text{Total}} = \frac{1}{2} \sum_{ij} \phi_{ij}(\mathbf{r}_{ij}) + \sum_{ij} F_i(\rho_i) \quad \text{Equation 1}$$

$$\rho_i = \sum_{j \neq i} \Psi_{ij}(\mathbf{r}_{ij}) \quad \text{Equation 2}$$

Where  $\phi_{ij}(\mathbf{r}_{ij})$  are two-body terms and  $F_i(\rho_i)$  are many-body terms that depend on the electron density of the metallic system. This electron density is calculated as the sum of the contribution of atoms within a given cutoff, which in many cases only consider first neighbours. There are several choices for selecting the functional dependence for the EAM implementation. Here we use that of Johnson,<sup>19</sup> since in our preliminary calculation of the Coefficient of Thermal Expansion (CTE) of Ni with several published interatomic potential was the one with better performance. Details in this regard are presented below in the Results section.

In the Johnson-type EAM potentials the terms are described as follows:

$$\phi_{ij}(\mathbf{r}_{ij}) = A e^{r_{ij}/d} - \frac{C}{r_{ij}^6} \quad \text{Equation 3}$$

$$F_i(\rho_i) = - \sum_{i,j} E_c \left[ 1 - \ln(\rho_i/\rho_0) \right]^{\alpha_j/\beta} (\rho_i/\rho_0)^{\alpha_j/\beta} + F_1(\rho_i/\rho_0)^{\gamma/\beta} \quad \text{Equation 4}$$

$$\rho_i = \sum_{i,j} A_d e^{B_d(r_{ij}-r_0)} \quad \text{Equation 5}$$

Where  $E_c$  is the cohesive energy,  $\alpha_j = 3(\Omega B/E_c)$ , (with  $\Omega$  as the volume per atom, and  $B$  as the bulk modulus) and  $r_0$  is the first nearest neighbour distance,  $a/\sqrt{2}$  for an fcc metal where  $a$  is the lattice parameter. The rest of them are fitted parameters. Note that it consists of two parameters in the two-body term ( $\phi$ ), six in the functional form (F), and the last three in the electron density function ( $\rho$ ). So, within this approach eleven parameters are therefore needed to model an elemental metal solid, three of which can be calculated directly from observables, namely  $E_c$ ,  $\alpha_j$ , and  $r_0$ .

For Ni, the cell parameter calculated with the original Johnson potential does not compare well with experiments (Table 1), and therefore this requires further improvements for a better description of the Ni alloys, mainly if predictive calculations are intended to be used to improve our understanding of structural and dynamical properties. For the parameterization there are six experimental observables, and therefore it is not possible to do the fitting in a straight way. Another important point preventing the fitting of the potentials in one step is that there are several

parameters that are largely correlated and therefore least square minimization with respect to observables is likely to fail if the starting parameters are not close to the optimal ones. In order to overcome these limitations, we developed an iterative procedure that relies on the optimization of a likelihood fitness function defined by us, as will be shown below.

It is known that Cr does not adopt an fcc structure, but a bcc one, and thus there are not experimental observables to be used for fitting fcc Cr. Then, we turned to the calculation of ab-initio observables that we can obtain through electronic structure calculations. However, ab-initio calculation of the elastic constants of Cr in fcc structure fails to provide reliable data, as the energy well of the relaxed fcc structure is so small that any tiny structural deviation pushes the system out from the energy well, resulting in negative elastic constants. We then used the extrapolated experimental data to pure Cr in fcc structure reported elsewhere.<sup>20</sup> Ni-Cr alloys exhibit fcc structures, as they are dominated by the larger content of Ni over Cr. For the parameterization of the interatomic potentials for the alloys only two parameters are needed to be fitted in the Johnson EAM scheme, those of the Buckingham term considering  $C$  equal to zero. The available experimental data were used for their determination.

To study the structural behaviour at finite temperatures MD simulations have been carried out using the LAMMPS code.<sup>21</sup> The time step is 1 fs, while the values of the thermostat and barostat parameters are 0.1 and 2.0 ps respectively. Simulations were performed for bulk (in the NPT ensemble) and nanoparticles (in the NVT ensemble) systems, for pure Ni and Ni-Cr alloys. The Cr contents studied were 10, 20, 30, and 40 %. The bulk systems were made of 15x15x15 unit cells, with 13500 atoms, whereas the nanoparticles radii were 3 nm, 5 nm, 7 nm, and 10 nm, with 1289, 5979, 16415, and 47741 atoms, respectively.

As a validation of the parameterized potentials we computed via ab-initio methods the cell variations with applied external hydrostatic pressure (from -20 to 100 GPa) and also the cohesive energy corresponding to each structure. For this purpose we used the VASP code.<sup>22</sup> We have employed the PBE exchange-correlation functional because it has been demonstrated that it is the functional that models transition metals more accurately.<sup>23</sup> The Brillouin zone has been sampled using a 14x14x14 Monkhorst-Pack K-point mesh for the calculations of the systems with only one unit cell. This is the grid that shows the best compromise between accuracy and computational cost. The mesh employed in systems with 2x2x2 unit cells was a 2x2x2 K-point mesh. The cut-off energy was 500 eV. It is important to note that magnetism has been taken into account for both pure metals differently, treating Ni as ferromagnetic and Cr as antiferromagnetic.

It is useful to mention that we tried to fit the potential parameters to ab-initio surface energy curves, but it resulted unsuccessful, even if only small deviations were scanned around the energy minimum. This is a limitation of the classical potential energy functional that is unable to capture with the necessary details the complex energetic behaviour of the metals, mainly Ni, under deformation. Nevertheless, as it will be shown below, the fit of the observables

provides a set of potentials parameters that reproduce well the targeted values.

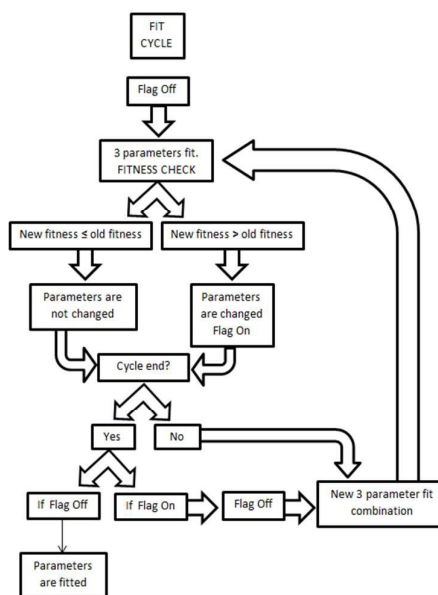
### 3 Results and Discussion

#### 3.1 Development of the interatomic potentials to model bulk Ni-Cr alloys.

The key point of our procedure for fitting the Ni potentials is based on the use of the code Gulp<sup>24, 25</sup> for fitting a reduced number of parameters in wisely designed cycles, until all parameters are modified and then repeated until convergence. This code has implemented the procedures to perform potential fittings, using least squares algorithms. It is important to notice that the complex nature of the metallic bonds hinders the development of classical potentials that perform well at reproducing at the same time structural observables, CTEs, and elastic constants. In this regard, we assigned weights to each calculated observable as compared with experiments in order to construct the fitness function in a way that allows measuring the progress of the overall quality of the fitting process. The procedure we followed to carry out the fitting of the potential parameters is shown in Scheme 1a. The procedure is outlined below:

1. A flag indicates if the fitness is being improved or not. Flag is set off at the beginning.
2. The first step is to check the fitness in the system with the starting parameters.
3. In each cycle, a number of optimization steps are conducted, where in each case only three parameters are optimized by a least squares optimization. Three parameters are taken, one from each term conforming the potentials (eq. 3 to 5), and the number of sets chosen is enough to make sure that all possible combinations of three parameters are considered.
4. If the new fitness is better than the best one obtained before, the new parameters will substitute the best ones; and if not, they are kept unchanged. If the potential is improved in one of the steps of a cycle, flag will be set on.
5. If the cycle has not ended, it will go back to the three parameters fit with a new three parameter combination.
6. If the cycle has ended, it will come back to start a new cycle just if the flag is on; if the flag is off, it means that in the last cycle the potential has not improved, so the algorithm will end.

We have made the fitness calculation according to a threshold tolerance (TT) and a weight for each observable as we show in Scheme 1b. They indicate us the error range that we are able to accept and the importance of each one in the final sum of fitness respectively. The relative value calculated for each observable depends on the comparison between the experimental value and the fitted one.



a)

**FITNESS CHECK**

TT ( $E_c$ )=12	weight ( $E_c$ )=1
TT ( $a$ )=8	weight ( $a$ )=1
TT ( $B$ )=12	weight ( $B$ )=0.75
TT ( $C_{11}$ )=32	weight ( $C_{11}$ )=0.5
TT ( $C_{12}$ )=32	weight ( $C_{12}$ )=0.5
TT ( $C_{44}$ )=32	weight ( $C_{44}$ )=0.5

$$relative.value_i = \frac{|fit.value_i - experimental.value_i|}{experimental.value_i} \cdot 100 \cdot \frac{1}{TT_i}$$

$$partial.fitness_i = f(relative.value_i)$$

$$fitness = \sum_{i=1}^6 weight_i \cdot partial.fitness_i$$

b)

**Scheme 1.** a) Algorithm developed to carry out the fitting of the potential parameters. b) Algorithm developed to calculate the fitness function.

Once the potentials parameters for Ni have been optimized, we find a much better agreement between calculated and experimental static properties than that obtained with the original Johnson potentials, and a level of agreement similar to that of other published potentials (see Table 1). We then studied the dynamic properties of the system. In Figure 1 the cell parameters of Ni as a function of the temperature are plotted. The newly developed interatomic potential is able to predict the variation with temperature of the cell parameters within an error of the order of 0.01 Å, while the errors obtained with the potentials developed by Bonny et al. increase as temperature increases, reaching 0.04 Å at 800 K. We have not included in Figure 1 the behaviour of the cell parameters as calculated with the MEAM interatomic potential, because this set of potentials, although providing excellent static properties, results in large structural instability of the simulation cell in NPT MD simulation, i.e. thermal motion causes the structure to deform, losing the cubic symmetry and giving rise to unphysical structures.

Table 1. Experimental<sup>26</sup> and simulated<sup>19, 20, 27, 28</sup> static observables (cohesive energy, lattice parameter, elastic constants, and bulk modulus) and CTEs of bulk fcc Ni.

<i>fcc Ni</i>	<i>Exp.</i> <sup>26</sup>	<i>Johnson</i> <sup>19</sup>	<i>Bonny</i> <sup>20</sup>	<i>Sutton Chen</i> <sup>27</sup>	<i>MEAM</i> <sup>28</sup>	<i>This work</i>
$E_c$ ( $\frac{eV}{atom}$ )	-4.45	-4.75	-4.45	-4.43	-4.45	-4.45
$a$ (Å)	3.519	3.433	3.519	3.521	3.521	3.519
$B$ (GPa)	179	167	179	195	181	179
$C_{11}$ (GPa)	247	230	247	231	247	235
$C_{12}$ (GPa)	147	134	147	177	148	151
$C_{44}$ (GPa)	125	157	125	80	125	131
$\alpha_{300K}$ ( $10^{-6}K^{-1}$ )	15.4	16.3	3.4	21.3	5.3	16.1

The new potential also provides an improved description of the variation with temperature of the CTEs, which vary from  $15.3 \cdot 10^{-6} K^{-1}$  to  $18.8 \cdot 10^{-6} K^{-1}$  in the temperature interval from 100 K to 1000 K, while the experimental CTEs change from  $14.1 \cdot 10^{-6} K^{-1}$  to  $17.6 \cdot 10^{-6} K^{-1}$ . This is in contrast to the previous well accepted potential for Ni-Cr systems<sup>20</sup>, which predicts CTEs that are too low in the range of temperatures studied, and that rises too quickly as temperature increases.

Since Ni is the most abundant metal in most Ni-Cr alloys of industrial relevance, the improvements that the new interatomic potentials yield at modelling bulk Ni will be of help when modelling structural and mechanical properties of Ni-Cr alloys. In Table 2 we show the static observables for bulk Cr. It must be noted that bulk Cr is not stable with an fcc structure, so there are no direct experimental data available of fcc Cr. Nevertheless, Smith and Was<sup>29</sup> extrapolated the data for pure fcc Cr, using values from various Ni-Cr alloys, of increasing percentage of Cr. These are the data presented in Table 2. It is observed that the agreement between the data obtained with the new potentials and the extrapolated experimental values is very good.

Once the potentials for modelling fcc Ni and Cr separately were available, we proceeded to fit the potential to model Ni-Cr alloys with a Ni/Cr ratio of 75/25. The results obtained for the calculated static properties of a Ni-Cr alloy with a Ni/Cr ratio of 80/20 are shown in Table 3, where we observe that the new Ni-Cr potentials reproduce well the experimental observables. Note that the quality of the fit with respect to the static observables for pure Cr is comparable to that of previous interatomic potentials<sup>20</sup>, while the results for Ni-Cr are largely improved with our potential.

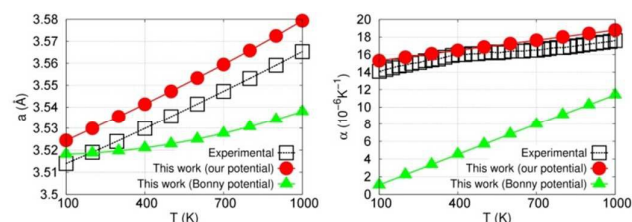


Figure 1. Experimental and calculated lattice parameters and CTE for fcc Ni, as a function of temperature.

Table 2. Extrapolated experimental<sup>29</sup> and simulated static observables (cohesive energy, lattice parameter, elastic constants, and bulk modulus) of bulk fcc Cr.

<i>Cr fcc</i>	<i>Exp.</i> <sup>29</sup>	<i>Bonny</i> <sup>20</sup>	<i>This work</i>
$E_c$ ( $\frac{eV}{atom}$ )	-3.69	-3.69	-3.72
$a$ (Å)	3.619	3.619	3.619
$B$ (GPa)	202	202	202
$C_{11}$ (GPa)	249	249	257
$C_{12}$ (GPa)	178	178	174
$C_{44}$ (GPa)	143	143	139

Table 3. Experimental<sup>30-32</sup> and simulated static observables (lattice parameter, elastic constants, and bulk modulus) of fcc Ni-Cr with a Ni/Cr ratio of 80/20.

<i>fcc Ni-Cr</i>	<i>Exp.</i> <sup>30-32</sup>	<i>This work Bonny Potentials</i> <sup>20</sup>	<i>This work Our Potentials</i>
$a$ (Å)	3.555	3.554	3.552
$B$ (GPa)	185	154	196
$C_{11}$ (GPa)	247	197	251
$C_{12}$ (GPa)	154	132	168
$C_{44}$ (GPa)	128	107	132

The fitted potentials parameters obtained in this work are reported in Table 4. Their use also provides better results than previous potentials when modelling the thermal behaviour of Ni-Cr solids, as can be seen in Figure 2. In particular, the curve of the variation of the cell parameter with temperature is close to the experimental results (the difference is of the order of 0.01 Å) and changes in a similar manner; while the curve obtained with previous potentials diverges from the experimental values as temperature increases. The behaviour of the CTE is similar to that observed for Ni; the new potential predicts values that are closer to experiment and vary with temperature in a similar fashion.

Table 4. Johnson-type EAM fitted parameters for fcc Ni, Cr, and Ni-Cr alloys.

<i>Buckingham</i>			
<i>Parameter</i>	<i>Ni-Ni</i>	<i>Ni-Cr</i>	<i>Cr-Cr</i>
$A$	6393.86	6675.50	5804.36
$\rho$	0.27829	0.27759	0.27800
<i>Johnson EAM functional</i>			
<i>Parameter</i>	<i>Ni</i>	<i>Cr</i>	
$E_c$	4.45000	3.69000	
$F_1$	4.49058	4.93708	
$\rho_0$	4.83626	4.08507	
$\alpha_f$	5.09453	6.03694	
$\beta$	6.45654	6.32622	
$\gamma$	8.85297	8.89153	
<i>EAM density</i>			
<i>Parameter</i>	<i>Ni</i>	<i>Cr</i>	
$A$	0.42133	0.61852	
$B$	2.67635	2.13582	
$r_0$	2.48900	2.13582	

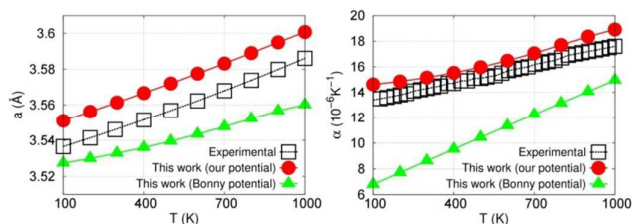


**Figure 2.** Experimental<sup>33</sup> and calculated lattice parameters (left) and CTEs (right) as a function of temperature for fcc Ni-Cr alloy with a Ni-Cr ratio of 80/20.

As a further rigorous structural test for the fitted interatomic potentials, we have made a comparison of the lattice parameters and the cohesive energies as a function of pressure, calculated with the potentials and with DFT calculations, for the three model systems (i.e. Ni, Cr, and Ni-Cr). Figure 3 shows that a successful reproduction of the DFT data is achieved with the new potentials. Note that the displacement of the enthalpy minimum as a consequence of the applied pressure is dictated by the curvature of the surface energy, thus by doing so we are proving that this curvature is reproduced by the new potentials. This is valid even for distances well beyond that of the surface energy minimum, i.e. apart from the harmonic region that is used for the calculation of the elastic constants. The agreement of the computed cohesive energies using the potentials with respect to those calculated by DFT is also remarkable. Indeed, the fact that the structural behaviour is well described by the new potentials at interatomic distances belonging to the region of the anharmonic curvature of the surface energy is a solid base for validating the predictive character of our fitted potentials towards their use at higher temperatures and pressures.

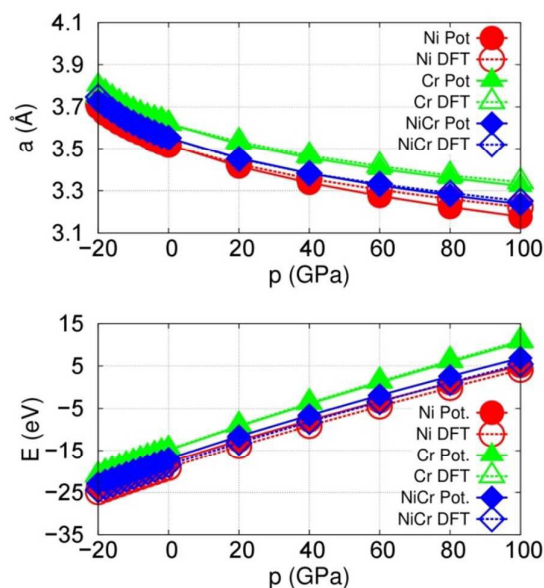


**Figure 3.** Dependence of the lattice parameters (left) and the cohesive energies (right) with the applied external pressure, calculated with the new potentials and with DFT calculations, for fcc Ni, Cr, and Ni-Cr 80/20.

### 3.2 Thermo-structural characterization of bulk Ni-Cr solids.

With the interatomic potential developed for Ni-Cr alloys we can predict the properties of Ni-Cr for which there are no experimental data. For example, Figure 4 shows the variation with temperature of the lattice parameters and CTEs, as well as the three elastic constants, for Ni-Cr alloys with Ni-Cr ratios of 100/0, 90/10, 80/20, 70/30, and 60/40.

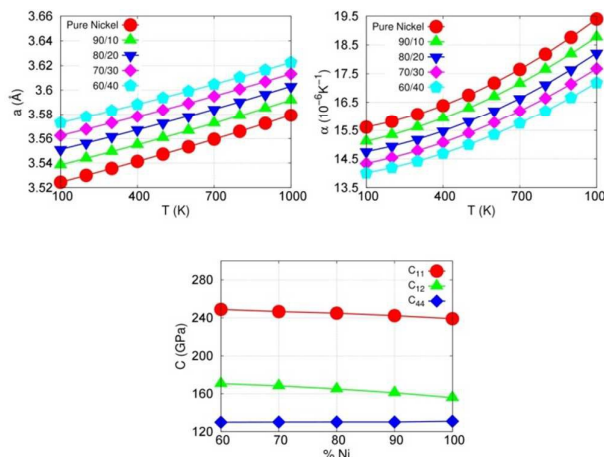


**Figure 4.** Calculated lattice parameters (top left) and CTEs (top right), as a function of temperature, as well as the three elastic constants (bottom), for Ni-Cr alloys of various compositions.

An interesting result is that the inclusion of Cr can decrease down to 10 % the CTEs, which would be a point to take into account when structural materials are designed for their use at high temperatures. It is also observed that the increase of the amount of Cr lowers the CTEs, which is in concordance with the smaller slope, in absolute values, of the cell parameter vs. pressure curves (Figure 3). The lattice parameters, as expected from the molar volume of each metal, increase as the amount of Cr increases. We found that by controlling the alloy composition the cell parameter can be tuned within an interval of 0.05 Å. It is also observed that the estimated C11 and C12 elastic constants decrease with the content of Ni, mainly C12, whereas C44 remains almost unaffected by the binary mixture composition.

### 3.3 Thermo-structural characterization of Ni-Cr nanoparticles.

Once we have tested the capability of the new interatomic potentials to model accurately bulk Ni-Cr, we use them to predict the thermo-structural properties of Ni-Cr nanoparticles of different sizes. We have studied 4 nanoparticles, whose diameters are 3 nm, 5 nm, 7 nm, and 10 nm (see Figure 5).

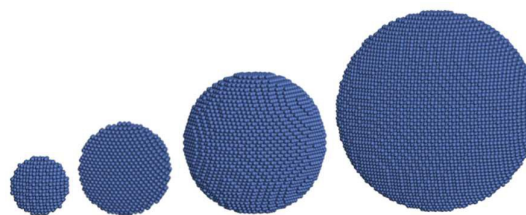


**Figure 5.** Ni nanoparticles with diameters of 3 nm, 5 nm, 7 nm, and 10 nm, from left to right. Ni-Cr nanoparticles of various Ni-Cr ratios have the same atomic positions, but have the corresponding percentage of Ni atoms exchanged with Cr atoms.

Their structures were generated by cutting spherical pieces of fcc Ni bulk crystal. It must be noted that these sizes are large enough so that most of the atoms are in the bulk, which means that the potential developed can be used without corrections.

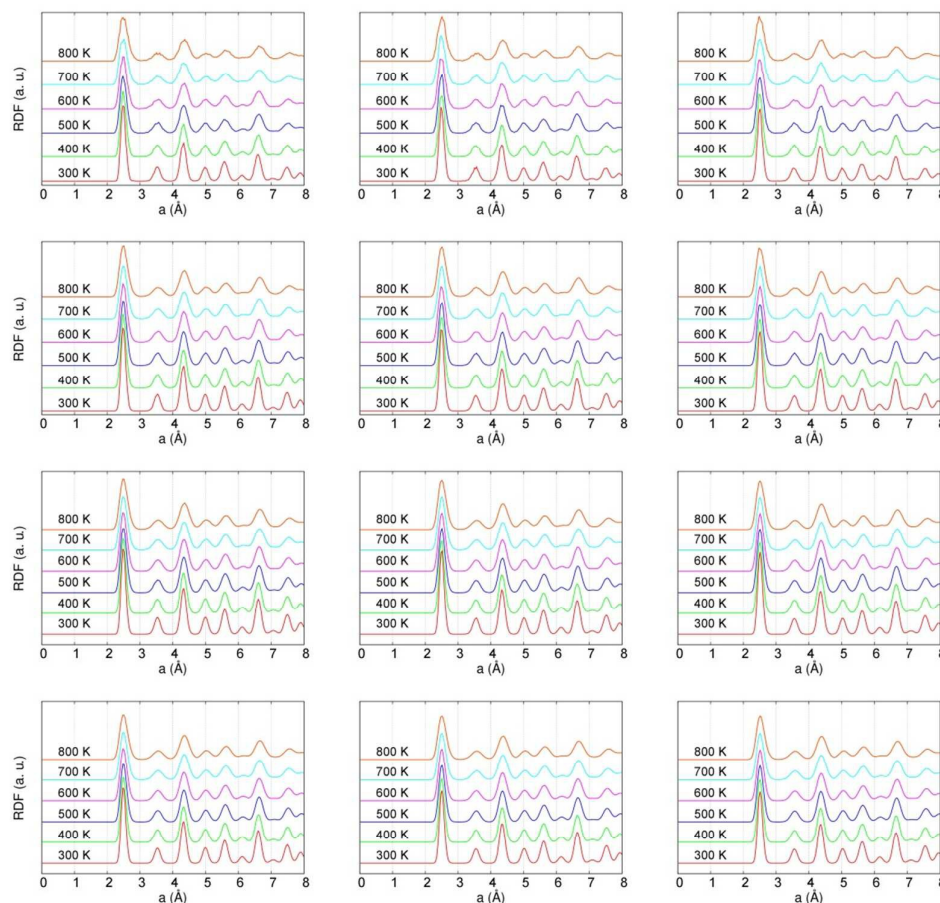


**Figure 6.** Ni-Ni RDFs of Ni-Cr nanoparticles of sizes (from top to bottom) 3 nm, 5 nm, 7 nm, and 10 nm. Left, middle, and right panels correspond to Ni-Cr ratios of 100/0, 90/10, and 80/20, respectively.

We have carried out MD simulations at temperatures between 300 K and 800 K, in order to study the influence of temperature on the structure of the nanoparticles. For each nanoparticle, we performed an initial energy minimization, after which we equilibrated the system during 30 ps at 800 K. Subsequently we carried out a production run, at that temperature, of 50 ps. The final structure was employed as a starting point of a new MD simulation, at 700 K, for which another equilibration run of 30 ps was performed, followed by a production run of 50 ps. This procedure continued until a final temperature of 300 K. The final structure at 300 K, for all nanoparticles, was crystalline, with very little disorder. This fact is reflected by the peaks of the Ni-Ni Radial Distribution Functions (RDFs) of the nanoparticles, which are shown in Figure 6, for all nanoparticle sizes, temperatures, and Ni-Cr ratios.

Our simulations show therefore that the crystalline structure of the nanoparticles is very resilient to changes in temperature, since even in this fast quenching of the systems highly ordered crystalline structures are readily attained. We mentioned previously the fact that all nanoparticles can be regarded as bulk-like nanoparticles, at least at room temperature, due to their large sizes. In order to check whether this is the case, we have studied the surface layer of the Ni nanoparticles, comparing the RDF of a 1 nm thick outer shell

with the RDF of the nanoparticle core (the rest of the nanoparticle), as well as with the RDF of the fcc Ni bulk structure, at 300 K. Since performing a MD simulation of the outer layer of the nanoparticle, without the core, would lead to unrealistic results, we have calculated the RDF of just the last structure of the simulations. The results (see S2 in Supplementary Information) show that all nanoparticles, even the smallest one show similar RDFs, which in turn are very similar to that of the bulk. Our simulations suggest that there are no large rearrangements of the surface layer of the nanoparticles.

Another interesting result from our simulations is that even at 800 K the nanoparticles get disordered, but still keep a high level of crystallinity. There is a big difference in this respect between the smaller nanoparticle (3 nm) and the rest. One way to analyse this different behaviour is calculating the Mean Squared Displacement (MSD) of the atoms of the nanoparticles. Figure 7 shows the MSDs of all nanoparticles, as a function of temperature. We observe that the 3 nm nanoparticles show the largest displacements of the atoms, and that there is very little difference between the rest of the nanoparticles, i.e. when the size reaches 5 nm the nanoparticles start having a bulk-like behaviour and an increase in size does not change drastically the dynamics of the atoms.

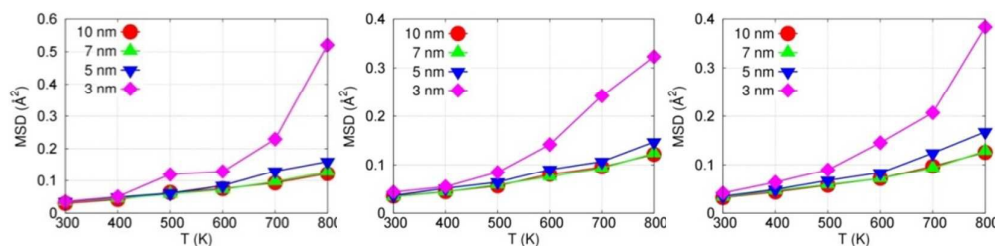


**Figure 7.** MSDs of the atoms of each nanoparticle, as a function of temperature, for Ni-Cr nanoparticles with Ni-Cr ratios, from left to right, of 100/0, 90/10, and 80/20.

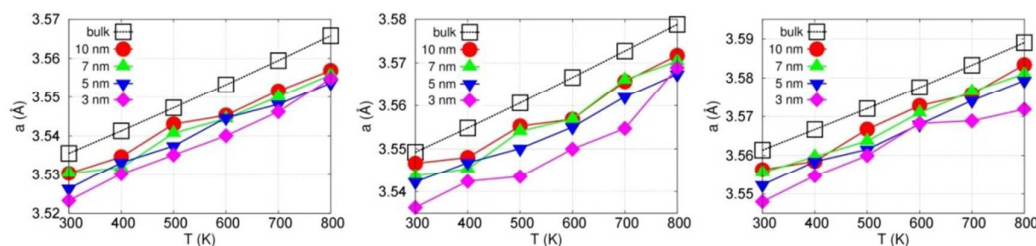


**Figure 8.** Variation with temperature of the cell size, for Ni-Cr nanoparticles with Ni-Cr ratios, from left to right, of 100/0, 90/10, and 80/20. The values obtained for the bulk are also shown, for comparison.

In order to study how the properties of the nanoparticles converge towards those of the bulk, we analysed the size of the unit cell. In order to calculate the size of the cells of the nanoparticles we made use of the RDFs. In the fcc structure the second peak of the RDF corresponds to the size of the unit cell, so we obtained the Gaussian that best fitted the second peak and calculated the unit cell size as the distance at which the Gaussian is centred. Using this method we were able to predict the variation of cell size for the nanoparticles, as a function of temperature (see Figure 8). We see that the cell sizes of the nanoparticles are slightly smaller than those of the bulk structure, for all temperatures, and that the variation with temperature has similar slope in all cases. The noise of the data could be due to the uncertainty in definition of a unique cell size for non-periodic structures such as the nanoparticles, as well as to the disorder associated with the presence of the surfaces.

As a final measure of the convergence of the properties of the nanoparticles we analysed potential energy as a function of size. The potential energy per atom of the nanoparticles at 300 K, as a function of size, is shown in Figure 9, left. We observe the expected decrease of energy as the size increases, for all Ni-Cr compositions. On the right we plot the same energies, but as a function of the inverse of the size. With this type of plot we see that, for each composition, all the energies are placed in a line, and that the line reaches the y axis at a value which is very close to that calculated for the bulk structure with the corresponding composition. For example, the line extrapolated for the pure nickel nanoparticles reaches the y axis when the energy is -4.40 eV/atom, exactly the same value obtained for the pure nickel bulk structure. We must note that the experimental cohesive energy of fcc Ni is -4.45 eV/atom, which differs from this value due to the increase of potential energy of the system associated with the thermal motion at 300 K.

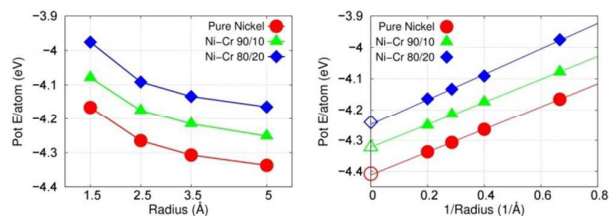


**Figure 9.** Left, potential energy per atom of the nanoparticles at 300 K, as a function of size. Right, potential energy per atom of the nanoparticles at 300 K, as a function of the inverse of the size. The energies per atom of the bulk structures are also shown on the right panel, over the y axis (open symbols).

As mentioned above, changes in state of aggregation of the nanoparticles can induce changes in the properties of the materials.<sup>34</sup> We have employed the new Ni-Cr potential to model the sintering of nanoparticles. Since we have not observed so far large differences between the behaviour of the nanoparticles of different sizes, we did not study the sintering of nanoparticles of all sizes. We decided instead to study the sintering of two 5 nm nanoparticles, with Ni-Cr ratios of 100/0 and 80/20, at two different temperatures (300 K and 1000 K). To do that, we placed initially the two nanoparticles in contact, at a distance of 2.49 Å, which is the distance between first neighbours in the bulk structure of fcc Ni. The systems were energy minimized, after which an equilibration of 30 ps was carried out, followed by a production run of 500 ps. Figure 10 shows snapshots at the beginning of the simulations (at 10 ps) and at the end (at 500 ps).

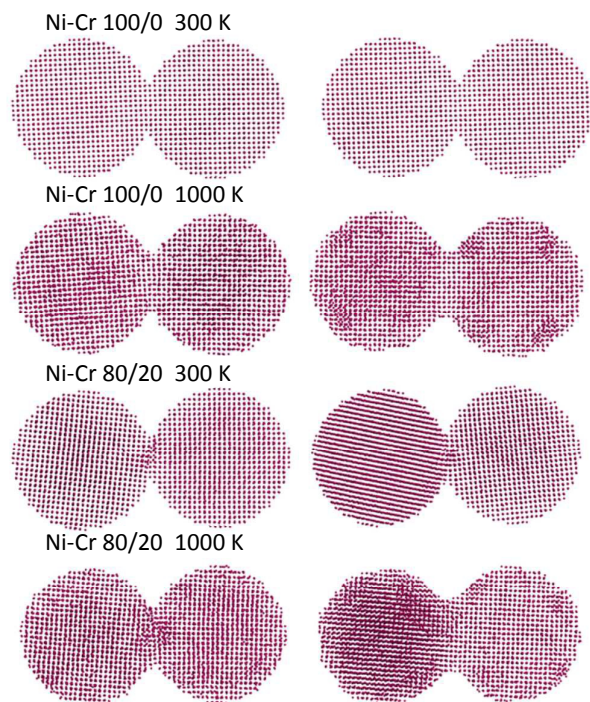


Figure 10 Snapshots of the simulations of the sintering process between two 5 nm nanoparticles structures, taken at 10 ps (left) and 500 ps (right). The Ni/Cr ratios and temperatures of the simulations are, from top to bottom 100/0 300 K, 100/0 1000 K, 80/20 300 K, and 80/20 1000 K.

We observe that for both types of nanoparticles (pure nickel and Ni-Cr alloy with Ni-Cr ratio of 80/20) there is no loss of crystallinity at 300 K, and the contact zones do not suffer significant changes. The main change is observed for the Ni-Cr 80/20 nanoparticles, which undergo a slight rotation in order to release some stress (see Figure 10c). The simulations at 1000 K show that, as expected, there is more disorder in the structures associated to the higher level of thermal motion. But this thermal motion is not enough to induce the fusion of the two nanoparticles and form a single larger nanoparticle. The contact zone is larger than in the simulations at 300 K, but it is still possible to regard the systems as formed by two nanoparticles in contact, so that the surface/volume ratio is similar to that a 300 K. Therefore, our simulations suggest that Ni-Cr nanoparticles also show the thermal stability that is characteristic of bulk Ni-Cr materials.

## Conclusions

We have fitted a new set of interatomic potential parameters that model the thermo-structural properties, including the mechanical properties, of Ni-Cr alloys. To do that, we have developed a fitting algorithm that uses a set of experimental observables. The fitted potential models correctly described the dependence with temperature of the lattice parameters and the coefficients of thermal expansion, for fcc Ni and Ni-Cr solids. The new potential has also been used to predict the properties of Ni-Cr materials of various compositions. Finally, we have used the new potential to study the behaviour of

nanoparticles of various sizes (3 nm, 5 nm, 7 nm, and 10 nm), finding that the lattice parameter increases as the size increases. The smallest nanoparticles (3 nm) behave differently from the others, i.e. when the size reaches 5 nm the nanoparticles show significant bulk-like features, although 3 nm nanoparticles are large enough to have a bulk-like core structure and show small surface distortions. Finally, the MD simulations of the sintering process show that when two 5 nm nanoparticles are in contact, they keep their structures as two separated nanoparticles, with a contact region in the middle, suggesting that materials made of nanoparticles of Ni-Cr alloys as small as 5 nm are quite resilient to thermally-induced damage and therefore capable of being used in applications such as catalysis, where high temperatures and aggressive environments are common.

## Acknowledgements

The authors want to acknowledge funding from the Virtual Materials Design (VMD) project by Abengoa Research. I.M.B. wants to acknowledge partial funding from the "Subprograma Ramón y Cajal" fellowship RYC-2012-10639 by the Spanish Ministry of Economy and Competitiveness. We thank the "Centro Informático Científico de Andalucía" (CICA) for providing partial of the computational resources needed to carry out this work.

## Notes and references

1. M. I. Besson, P. Gallezot and C. Pinel, *Chemical Reviews*, 2013, **114**, 1827-1870.
2. R. Ferrando, J. Jellinek and R. L. Johnston, *Chemical Reviews*, 2008, **108**, 845-910.
3. R. L. Johnston and J. P. Wilcoxon, *Metal nanoparticles and nanoalloys*, Elsevier, 2012.
4. G. W. Meetham and M. H. Van de Voorde, in *Materials for High Temperature Engineering Applications*, Springer, 2000, pp. 68-82.
5. Z. Gentry, A. Sakamoto, M. Corey, N. Thongchua and K. Patel, 2014.
6. A. Vita, G. Cristiano, C. Italiano, L. Pino and S. Specchia, *Applied Catalysis B: Environmental*, 2015, **162**, 551-563.
7. K. Sato, K. Kawano, A. Ito, Y. Takita and K. Nagaoka, *ChemSusChem*, 2010, **3**, 1364-1366.
8. H. Inokawa, T. Ichikawa and H. Miyaoka, *Applied Catalysis A: General*, 2015, **491**, 184-188.
9. H. C. Yu, X. Y. Huang, F. H. Lei, X. C. Tan, Y. C. Wei and H. Li, *Electrochimica Acta*, 2014, **141**, 45-50.
10. W. Qu, L. Zhang and G. Chen, *Biosensors and Bioelectronics*, 2013, **42**, 430-433.
11. S.-H. Park and H.-S. Kim, *Thin Solid Films*, 2014, **550**, 575-581.
12. Y. K. Moon, J. K. Lee, J. G. Kim, M. Y. Jung, J. B. Lee and S. H. Kim, *Current Applied Physics*, 2009, **9**, 928-932.
13. J. Lif, M. Skoglundh and L. Löwendahl, *Applied Catalysis A: General*, 2002, **228**, 145-154.

14. J. Sehested, J. A. Gelten and S. Helveg, *Applied Catalysis A: General*, 2006, **309**, 237-246.
15. J. Perelaer, P. J. Smith, D. Mager, D. Soltman, S. K. Volkman, V. Subramanian, J. G. Korvink and U. S. Schubert, *Journal of Materials Chemistry*, 2010, **20**, 8446-8453.
16. J. R. Weertman, *William Andrew Publishing, 13 Eaton Avenue, Norwich, NY 13815, USA, 2002.*, 2002, 397-421.
17. J. Li, X. Dai, S. Liang, K. Tai, Y. Kong and B. Liu, *Physics Reports*, 2008, **455**, 1-134.
18. Y. Mishin, M. Mehl and D. Papaconstantopoulos, *Physical Review B*, 2002, **65**, 224114.
19. R. Johnson, *Physical Review B*, 1989, **39**, 12554.
20. G. Bonny, D. Terentyev, R. Pasianot, S. Poncé and A. Bakaev, *Model. Simul. Mater. Sci. Eng.*, 2011, **19**, 085008.
21. S. Plimpton, P. Crozier and A. Thompson, *Sandia National Laboratories*, 2007, **18**.
22. G. Kresse and J. Furthmüller, *Phys. Rev. B*, 1996, **54**, 169.
23. P. Janthon, S. M. Kozlov, F. Viñes, J. Limtrakul and F. Illas, *J. Chem. Theo. Comput.*, 2013, **9**, 1631-1640.
24. J. D. Gale, *Journal of the Chemical Society, Faraday Transactions*, 1997, **93**, 629-637.
25. J. D. Gale and A. L. Rohl, *Molecular Sim.*, 2003, **29**, 291-341.
26. G. Simmons and H. Wang, *Cambridge (MA): MITPress*, 1971.
27. A. Sutton and J. Chen, *Philosophical Magazine Letters*, 1990, **61**, 139-146.
28. M. Baskes, *Physical Review B*, 1992, **46**, 2727.
29. R. W. Smith and G. S. Was, *Physical Review B*, 1989, **40**, 10322.
30. F. Abe and T. Tanabe, *Z. Metallkd.*, 1985, **76**, 293-298.
31. L. Kaufman, *Calphad*, 1977, **1**, 1.
32. E. Lahteenkorva and J. Lenkkeri, *Journal of Physics F: Metal Physics*, 1981, **11**, 767.
33. B. Rabin, W. Swank and R. Wright, *Nuclear Engineering and Design*, 2013, **262**, 72-80.
34. A. J. Logsdail, N. J. Cookson, S. L. Horswell, Z. Wang, Z. Li and R. L. Johnston, *The Journal of Physical Chemistry C*, 2010, **114**, 21247-21251.